Research, Society and Development, v. 10, n. 12, e476101220855, 2021
(CC BY 4.0) | ISSN 2525-3409 | DOI: http://dx.doi.org/10.33448/rsd-v10i12.20855

Influence of the shaker mill in the properties of ZnO processed by high energy milling

Influência do moinho vibratório nas propriedades do ZnO processado por moagem de alta energia

Influencia del molino vibratorio en las propiedades del ZnO procesado por molienda de alta energía

Received: 09/21/2021 | Reviewed: 09/25/2021 | Accept: 09/26/2021| Published: 09/27/2021

Ana Gabriela Storion
ORCID: https://orcid.org/0000-0002-6099-4292
Universidade de São Paulo, Brazil
E-mail: anagstorion@usp.br
Eliria Maria de Jesus Agnolon Pallone
ORCID: https://orcid.org/0000-0002-6727-0545
Universidade de São Paulo, Brazil
E-mail: eliria@usp.br
Tania Regina Giraldi
ORCID: https://orcid.org/0000-0002-4627-8118
Universidade Federal de Alfenas, Brazil
E-mail: tania.giraldi@unifal-mg.edu.br
Sylma Carvalho Maestrelli
ORCID: https://orcid.org/0000-0002-5037-4276
Universidade Federal de Alfenas, Brazil
E-mail: sylma.maestrelli@unifal-mg.edu.br

Abstract

This work evaluates how the High Energy Ball Milling (HEBM) in a shaker mill influences the optical, physical, and microstructural properties of ZnO. The procedure also combines Fe inclusion from the grinding medium with particle size reduction. ZnO powder was milled by 1, 2, 3, 4, and 5 h, which resulted in a particle size reduction to the nanometric scale with a mean size of around 50 nm and a crystallite size reduction by three times when processed from 4 h. Milling has proven to be an efficient process for obtaining nanoparticles with an incredibly short processing time and changed the morphology of the particles from random to spherical shapes. Results also indicate the processing progressively expanded the ZnO hexagonal structure due to the imposed strain and Fe inclusion, which can help to decrease the bandgap and slow down the recombination rate of the electron-hole pairs, improving the photocatalysis activity. The optical results showed no additional band appeared due to milling processes and diminished the bandgap from 3.37 to 3.21 eV. Milling also led to an increase in the c value from 5.2076 to 5.2112 Å, which is one of the most important factors for improved antibacterial activity. HEBM has proved to be a suitable process for obtaining ZnO nanoparticles with properties useful for various applications.

Keywords: High energy milling; Nanoparticles; Zinc oxide, Rietveld refinement.

Resumo

Este trabalho avalia como a Moagem de Alta Energia (MAE) em um moinho vibratório influencia as propriedades ópticas, físicas e microestruturais do ZnO. O procedimento também combina a inclusão de Fe do meio de moagem com a redução do tamanho da partícula. O pó de ZnO foi moído em 1, 2, 3, 4, e 5 h, o que resultou numa redução do tamanho das partículas à escala nanométrica com tamanho médio de cerca de 50 nm e uma redução do tamanho do cristalito em três vezes quando processado por 4 h. A moagem provou ser um processo eficiente para obter nanopartículas com um tempo de processamento incrivelmente curto e alterou a morfologia das partículas previamente aleatórias para esféricas. Os resultados indicam também que o processamento expandiu progressivamente a estrutura hexagonal ZnO devido à tensão imposta e à inclusão de Fe, o que pode ajudar a diminuir o band gap e a minimizar a taxa de recombinação dos pares elétron-buraco, melhorando a atividade de fotocatálise. Os resultados ópticos não mostraram qualquer banda adicional surgida na processos de moagem e uma diminuição do band gap de 3,37 para 3,21 eV. A moagem também levou a um aumento do valor c de 5,2076 para 5,2112 Å, o que é um dos fatores mais importantes para a melhoria da atividade antibacteriana. A MAE provou ser um processo adequado para a obtenção de nanopartículas de ZnO com propriedades úteis para várias aplicações.

Palavras-chave: Moagem de alta energia; Nanopartículas; Óxido de Zinco, Refinamento de Rietveld.

Resumen

Este trabajo evalúa cómo la molienda de bolas de alta energía (MAE) en un molino agitador influye en las propiedades ópticas, físicas y microestructurales del ZnO. El procedimiento también combina la inclusión de Fe del medio de molienda con la reducción del tamaño de las partículas. El ZnO fue molido durante 1, 2, 3, 4 y 5 h, lo que resultó en una reducción del tamaño de las partículas hasta la escala nanométrica, con un tamaño medio en torno a los 50 nm, y a una reducción del tamaño de los cristalitos tres veces mayor cuando se procesó a partir de las 4 h. La molienda demostró ser un proceso eficaz para obtener nanopartículas con un tiempo de procesamiento increíblemente corto y cambió la morfología de las partículas de formas aleatorias hasta esféricas. Los resultados también indican que el procesamiento amplió progresivamente la estructura hexagonal del ZnO debido a la tensión impuesta y a la inclusión de Fe, lo que puede ayudar a disminuir el bandgap y a reducir la tasa de recombinación de los pares electrón-hueco, mejorando la actividad de fotocatálisis. Los resultados ópticos mostraron que no apareció ninguna banda adicional y una disminución del bandgap de 3,37 a 3,21 eV. MAE también condujo a un aumento del valor c de 5,2076 a 5,2112 Å, que es uno de los factores más importantes para mejorar la actividad antibacteriana. El HEBM ha demostrado ser un proceso adecuado para la obtención de nanopartículas de ZnO con propiedades útiles para diversas aplicaciones.

Palabras clave: Molienda de alta energía; Nanopartículas; Óxido de Zinc, Refinamiento Rietveld.

1. Introduction

ZnO is a ceramic material and II-VI semiconductor (as it is formed by a metallic IIB and a non-metallic VIA element), with n-type semiconduction. It has a wide band gap (Eg = 3.37 eV) and high exciton binding energy (60 meV) at room temperature (Fan, Sreekanth, Xie, Chang, & Rao, 2013; Samavati et al., 2021; Toporovska et al., 2020). These characteristics make it interesting for several applications in electronic and optoelectronic devices, such as lasers, sensors, photocatalysts, solar cells, transistors, and antibacterial materials, as they can be activated by UV light to release reactive oxygen species in an aqueous solution (Noman, Amor, & Petru, 2021; Otis, Ejgenberg, & Mastai, 2021; Wang, Zhu, Huang, Mei, & Jia, 2019). Among the possible crystalline defects in the structure of pure ZnO (O vacancy, Zn vacancy, interstitial Zn, interstitial O, substitutional Zn), interstitial O and Zn vacancies are the most frequent, which leads to the predominance of n-type semiconduction without the need for external doping (Fan et al., 2013). Most binary semiconductors II-VI crystallize in cubic zinc blende and/or hexagonal wurtzite structures, where the tetrahedron is formed by one anion surrounded by four cations at the corners (Morkoç & Özgür, 2009). This structure provides a mixed character between ionic and covalent, which raises the bandgap energy above that expected when only covalent bonds are present. For ZnO, the possible crystal structures are, besides the zinc blende and the wurtzite, the cubic rock-salt structure. Under normal temperature and pressure conditions, wurtzite is the most thermodynamically stable crystal structure. The zinc blend is metastable and obtainable under specific processing conditions. Similarly, rock-salt can only be obtained under high pressure, so that the interaction between the atoms is forced as much as possible to become predominantly ionic (Lee, Lai, Ngai, & Juan, 2016; Morkoç & Özgür, 2009).

The properties of ZnO are widely attributed to its particle size, the amount of the grains and grain boundaries (Aimable, Goure Doubi, Stuer, Zhao, & Bowen, 2017; QIN, SHAO, LIU, & WANG, 2005) and also the concentration of defects (B. Chen, Xia, & Lu, 2013; Lott et al., 2015) Thus, electrical and optical properties of ZnO have been improved by maintaining its nanometer-scale microstructure (Lee et al., 2016). The interest in nanostructured materials is growing due to the gain in several properties, such as optical, mechanical and catalytic, among others (Aimable et al., 2017; Phuah, Rheinheimer, Akriti, Dou, & Wang, 2021; Samavati et al., 2021). By starting the processing step with a nanoscale material, it is possible to refine the microstructure. With refinement, several interesting properties can be controlled, such as electrical properties (due to higher electron mobility), optical properties (due to access to a wider range of radiation absorption), mechanical properties, among others (Choi, Jung, Shin, & Sohn, 2015; Lee et al., 2016; Lott et al., 2015; Phuah et al., 2021; Samavati et al., 2021).

There are several techniques for obtaining semiconductor powders in nanometric scale. The existing methods include chemical, thermophysical, mechanical synthesis, and mechanical milling, as in the case of high energy ball milling (HEBM) (Pawan Kumar & Kumar, 2021; Mayo, Hague, & Chen, 1993; Noman et al., 2021; Samavati et al., 2021). Among the high energy mills currently used in HEBM, it can be mentioned shaker mill, planetary ball mills, attritor mills, and commercial mills. They differ in capacity, milling efficiency, and additional systems for heating and cooling (Dutková et al., 2016; Suryanarayana, 2001). Shaker type mills movements cause friction between the balls inside the vial and ball-wall friction, promoting the mixing and grinding of the material under high impact forces, characterizing it as high energy (Suryanarayana, 2001). HEBM is a consolidated technique among the routes for obtaining fine powders (Dzik, Svoboda, Kaštyl, & Veselý, 2019). Also, it consists of a technique for doping ceramic oxides.

Some studies have reported applications of ball-milled powders (Bégin-Colin et al., 2009; Dias et al., 2016; Otis et al., 2021; Reddy et al., 2019; Šepelák, Bégin-Colin, & Le Caër, 2012). For ZnO semiconductors, besides other important properties such as size and surface area, the exposure surface and the surface defects play an important role in its applications (D. Chen et al., 2014; Zhang et al., 2014). ZnO nanoparticles increases the photocatalytic, antibacterial, and antimicrobial activity (Noman et al., 2021). Salah et al (2011) (Salah et al., 2011) firstly applied HEBM through a planetary mill up to 50h for reducing the particle size of ZnO to nanometric scale from a microcrystalline powder, suggesting the modifications induced in ZnO nanoparticles might prove useful as antibacterial material. Gancheva et al (2013) (Gancheva, Iordanova, Dimitriev, Avdeev, & Iliev, 2013) used the same milling to evaluate the photocatalytic activity of ZnO after milling for 10h with different milling speed rotation (Gancheva et al., 2013). Chen et al (2014) (D. Chen et al., 2014) stated that the defects promoted during HEBM highly influence the photocatalytic activity of ZnO with increased time and rotation due to the bulk defects promoted during the milling process. Mekprasart et al. (2020) (Mekprasart, Chutipaijit, Ravuri, & Pecharapa, 2020) evaluated different time of processing and milling rotation on the ZnO size reduction as a top-down process with high efficiency to achieving nanoparticles.

Additional to particle size reduction, the mechanic activation by milling processes was also applied to the incorporation of ions to improve the photocatalytic efficiency of ZnO (Kotha, Kumar, Dayman, & Panchakarla, 2021). This process can help decrease the bandgap and slow down the recombination rate of the electron-hole pairs. Güler et al (2016) (Güler, Güler, Evin, & Islak, 2016) investigated the influence of milling time and Fe2O3 content on the optical and electrical properties of ZnO and the results showed enhanced properties with potential for photocatalysis. Reddy et al (2019) (Reddy et al., 2019) evaluated the photocatalytic activity of Fe doped ZnO nanoparticles obtained by HEBM. The authors achieved high percentage of degradation using a milling time of 40h. Doping using several metal ions have also been used to enhance the ZnO optical and catalytic activity, such as Cu (Chandekar et al., 2020; Jiang et al., 2019), Co (Gonçalves, Paganini, Armillotta, Cerrato, & Calza, 2019), Fe (Reddy et al., 2019; Yin et al., 2017), among others (Khalid et al., 2019; Promod Kumar et al., 2020). Sharma et al (2016) (N. Sharma, Jandaik, & Kumar, 2016) also demonstrated that doping ZnO nanoparticles with Fe showed improved antimicrobial activity. Despite several works that have been made regarding the application of HEBM to ZnO, no discussion concerning shaker mills has been found in the literature.

The purpose of this study was to investigate the applicability of HEBM in the particle size reduction of the ZnO powder with an increase in the number of particles at a nanometer scale. Also, it aimed to investigate if the generation of higher surface area, until then unexposed, (one of the most important properties to evaluate in samples that have undergone milling processes) will influence on the ZnO's physical and optical properties. Since the milling was carried out in steel vial and ball, the incorporation of Fe ions was also analyzed.

2. Methodology

The present work consists of an experimental research based on a qualitative approach and the data were discussed on the lights of descriptive-diagnostic analysis. Zinc Oxide powder (ZnO, 99% purity, Synth®) was used as the material of study for the milling procedures. ZnO commercial was characterized by X-ray diffraction. The analyses were performed with Cu Kα radiation in 0.1542 nm, at 40 kV and 30 mA, scanning between 15 and 75 º with an angular step of 0.02º in continuous mode.

The powder was dry milled in a SPEX 8000 shaker/ Mill, in which hardened steel vial and ball (5 mm in diameter). The ball/powder mass ratio was 5:1, and the milling times were 1, 2, 3, 4, and 5 h, according to previous works (Pallone et al., 2010; Yokoyama, 2008). After finishing the milling process, the fine powder was leached with 0.5 M oxalic acid (Anidrol, analytical grade), for the removal of surface Fe from the grinding medium. The removal of the excess Fe residue will favor the analysis only of the interference of the ions incorporated in the ZnO. For the acid leaching, the ratio of 3 g of the powder to 100 mL of oxalic acid solution was used. The mixture was left under stirring and heating to approximately 100 ºC for 4 hours. After the leaching, the solution was kept at rest for the separation of the liquid, through the decanting of the powder. Once separated, the powder was led to another leach, so that the procedure was performed three times for each sample. After leaching, the powders were washed to remove the residual acid, by stirring and heating in distilled water for 30 minutes, repeating the procedure three times with water exchange at each repetition. Isopropyl alcohol was added after the last wash and drying, and the suspension was allowed to stir again for thirty minutes. The samples were then deagglomerated in isopropyl alcohol medium in Ultrasonic Sanders bath for 25 minutes and slow dried at 50ºC. After drying, the powder was sifted through a 45 µm opening sieve. The leaching procedure was adapted according to previous works (Hernández, García, Cruz, & Luévanos, 2013; Silva et al., 2008).

The milled powders were characterized by X-ray diffraction at the same condition as previously described. The crystallite average size was determined using the Williamson-Hall method. Assuming that the microstress is uniform in all crystallographic directions according to the uniform deformation model (UDM), Equations A is used for calculus (Mote, Purushotham, & Dole, 2012; Prabhu, Rao, Kumar, & Kumari, 2014; Williamson & Hall, 1953):

$$\beta * cos\theta = \frac{k\,\lambda}{D} + 4 * \varepsilon * sin\ \theta \qquad \text{(Eq. A)}$$

where β is the full width at half maximum of the diffracted peak (FWHM); θ is the Bragg diffraction angle; K is a shape value constant, dependent on the morphology of the particle; λ is the wavelength of the used radiation (Cu Kα = 0.1542 nm); ε is the component of crystalline microdeformations; D is the crystallites average size. From Equation A, when considering linear function y=ax+b, where y corresponds to β*cosθ and x to 4*sinθ, the angular coefficient of the linear adjustment performed for the experimental points will be equivalent to the microdeformation ε and the linear coefficient will correspond to (K*λ)/D.

Differential Scanning Calorimetry (DSC) and Thermogravimetric Analysis (TGA) were simultaneously carried out in a Netzsch Jupter STA 449F3 equipment, between 200 and 1100 ºC, under Nitrogen atmosphere, with a heating rate of 10 K/min. Also, Fourier Transform Infrared Spectrometry (FTIR) was performed in a Perkin-Elmer Spectrum 1000, with transmittance measurements performed in the range of 4000 to 450 cm^{-1}, with KBr-pressed samples.

Semi-quantitative chemical analysis via X-ray fluorescence (FRX) was performed using the Axios PW 4400/40 DY 1686 equipment. The beads for analysis were made using a lithium tetraborate (Li2B4O7) 99.5% fluxing agent and 0.5% lithium bromate (LiBr) using a platinum-gold crucible. The powder morphology and particle size were analyzed by scanning electron microscopy (SEM) in a Magellan 400 L equipment.

The optical analysis was evaluated by Diffuse Reflectance Spectroscopy (DRS), performed in a Varian Cary 5G spectrophotometer between 250 nm and 800 nm. The samples' optical band gap was calculated by the Tauc's Plot as described by Dias et al (2018) (Dias, Oliveira, Renda, & Morelli, 2018). For nomenclature purposes, the samples were prefixed Z followed by the processing time number. The ZnO as purchased is named ZnOP (pattern). The samples that underwent the leaching process received the suffix L. Also, some samples that underwent heat treatment received the terminology T followed by the used temperature. Heat treatments were carried out at temperatures of 600, 800, 900 and 1000 ºC. The analysis of the particle size distribution was performed by laser diffraction (Horiba - LA-950V2), in alcoholic medium, with prior 30 min in the ultrasound, considering the number of particles as distribution basis.

3. Results and Discussion

The results will be presented according to the characterization steps, corresponding to the precursor powder, then to the processing, and finally to the processed material. The results for X-ray diffraction of the precursor and milled powder are presented in Figure 1.

Figure 1 - X-ray diffractogram for (a) milled powders from 1 to 5 h and raw material, and the small peaks in evidence indicating the presence of Fe according to ICDD #6-696; (b) leached samples and respective pattern for hexagonal zinc oxide and hydrated zinc oxalate.

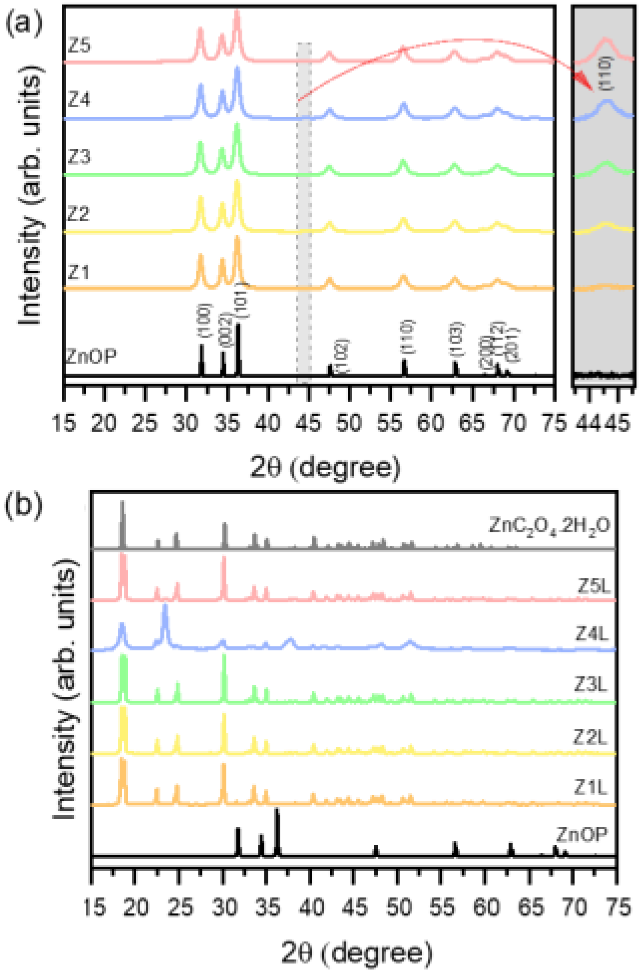

Source: Authors (2021).

According to Figure 1, the ZnOP (pattern) presented the hexagonal crystalline structure, corresponding to the mineral Wurtzite (ICDD #2003-6-1451). Figure 2 (a) shows the comparison of the diffractograms of the milled ZnO samples from 1 to 5 h and their respective precursor powder. It can be seen the main diffraction planes present in all samples. All diffractograms were identified according to the same precursor oxide card (ICDD #36-1451). As described in the literature (Dib, Trari, & Bessekhouad, 2020; Promod Kumar et al., 2020; Poornaprakash, Chalapathi, Subramanyam, Vattikuti, & Park, 2020), this crystalline structure corresponds to the active phase for most required ZnO applications. Small peaks (on the magnification of Figure 1 (a)) indicate Fe presence (ICDD # 6-696). The Fe peak intensity has increased following the increase in the milling time. The difference between the oxides before and after milling is related to the enlargement of the diffracted peaks for the milled samples.

Figure 1(b) shows the comparison of the diffractograms of the milled samples after the leaching process. Comparing the samples processed with the standard ZnO, it showed that these diffractograms no longer presented the peaks corresponding to zinc oxide. All leached compositions were identified as zinc oxalate hydrate ($ZnC_2O_4.2H_2O$), according to ICDD 2003 #25-1029. It was noticed, during the leaching process, that there was an interaction between the leached oxide and the leaching acid. In addition to zinc oxalate, Z4L sample presented the formation of an intermediate compound, with the respective diffracted peaks showing correspondences with the zinc oxalate (ZnC_2O_4 – ICDD #37-718) and zinc oxalate hydrate. Analyzing the diffractograms of the processed samples (Figure 1(a)), as the milling time increases, there is a crystallinity loss of the samples due to the induced deformations. The peak broadening may occur as a function of crystallite size decrease, lattice distortion and crystalline defects (Mote et al., 2012; Prabhu et al., 2014; Williamson & Hall, 1953). Table I describes the crystallite average size for each sample processed by HEBM according to the W-H method, where the crystallite size contribution to the peak broadening is calculated separately to the lattice strain.

Table 1 - Crystallite size calculated by Williamson-Hall method for the samples processed via HEBM compared to the ZnO pattern before processing.

Sample	ZnOP	Z1	Z2	Z3	Z4	Z5
Crystallite Size (nm)	113	69	52	46	35	32

Source: Authors (2021).

According to Table 1, the Williamson-Hall results indicate the increase in the milling time was accompanied by a decrease in the crystallite size. The crystallite size reduced until the 4-hour value has been reached, from which no significant differences were observed. The results show that the nanometric scale of the processed powders is likely to be obtained by HEBM, since very small crystallite sizes were reached. To better characterize the peak broadening and structure changes according to the milling time, Rietveld Refinement was performed for the non-leached oxides. The results are presented in Figure 2.

Figure 2 - Rietveld refinement results: adjusted profiles and experimental data for a) ZnOP and b) Z5, c) variation lattice parameters and volume according to the milling time.

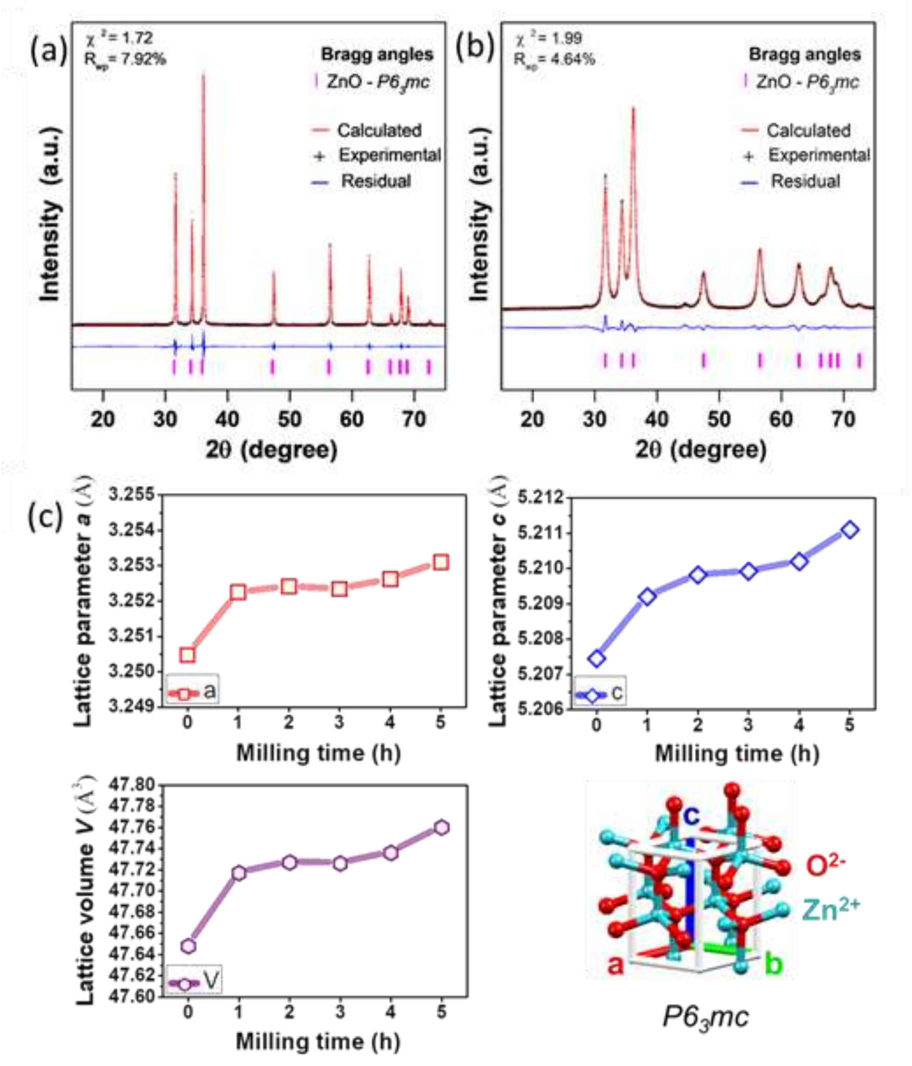

Source: Authors (2021).

Adequate adjusts were obtained, as exemplified for ZnOP (Fig. 3a) and Z5 (Fig. 3b). The residual between the calculated and experimental data shows a good refinement was achieved, and also the R_{wp} and χ^2 values show high-quality and trustworthy results. The hexagonal strucure was progressively expanded according to the milling time, since the lattice parameters a, c, and the structure volume V increased after processing, as shown in Figure 2(c). The structure was schematized in Fig.3c, utilizing the crystallographic coordinates from Schreyer at al. (Schreyer, Guo, Thirunahari, Gao, & Garland, 2014). The lattice suffered a greater expansion in the first hour. Next, the expansion continued occurring, but in a slower rate. This phenomenon can be attributed to two concomitant processes: the strain due to the impact and shear forces promoted by HEM; and the Fe cation structural inclusion from the vessel and milling spheres. The former occurred more intensively in the first hour, observed by a significant increment of the diffraction peaks broadening compared to the raw oxide. The latter is mainly attributed to the cationic structural inclusion, which can also lead to lattice expansion. Fe^{2+} has a larger crystal radius than Zn^{2+} in tetahedral coordination (0.77 Å versus 0.74 Å, respectively) (Saleh, Prakoso, & Fishli, 2012; Shannon, 2011), therefore, isovalent inclusions promoted the lattice expansion in a minor extent.

Many works have also reported the use of ZnO nanostructures as antibacterial material. Yamamoto et al (2004) stated that this effect can be increased when the c value is also increased (Yamamoto, Komatsu, Sawai, & Nakagawa, 2004). According to Rietveld analysis, the c value has increased from 5.2075 Å to 5.2112 Å. The increase in the c value typically leads to high amounts of H_2O_2 release which can inhibits bacterial growth. Salah et al (2011) were able to increase the c value of ZnO from 5.204 to 5.216 with 50h of milling in a horizontal oscillatory mill (Retsch, PM 400). Therefore, the use of a shaker mill might reduce the time of processing to produce ZnO with adequate characteristics for antibacterial applications.

FTIR was performed to identify the functional groups and chemical bonds present in the samples after leaching. Figure 3 shows the FTIR spectral referring to ZnOP and ZnO processed via HEBM and submitted to acid leaching and Table 2 shows the FTIR band assignments.

Figure 3 - FTIR transmittance spectrum for ZnOP sample compared to leached Z1L, Z2L, Z3L, Z4L, and Z5L samples.

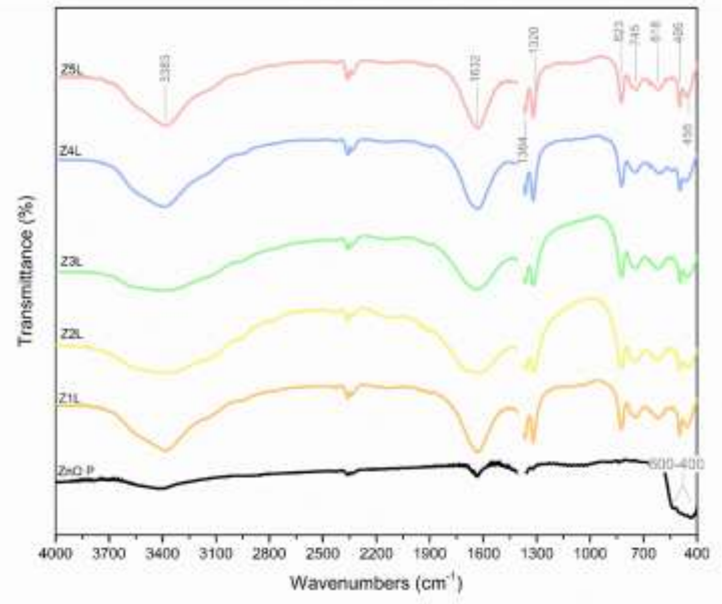

*the break in 1384cm^{-1} is related to the impurity band present in the KBr source used for sample pressing. Source: Authors (2021).

Table 2 - Relationship of the bands observed in the FTIR spectra for samples processed via HEBM and leached in oxalic acid and their assignments.

Wavenumber (cm^{-1})	Assignment
3383	v (OH) : H_2O(Wladimirsky1 et al., 2011)
1632	v_{as} (CO)(Cooper, 2015; Wladimirsky1 et al., 2011)
1364	v_s(CO) + v_s(CC)(Georgeta et al., 2015; Wladimirsky1 et al., 2011)
1320	v_s(CO) + δ(OCO)(Cooper, 2015; Georgeta et al., 2015)
823	v_s(CC) + δ(OCO)(Cooper, 2015; Wladimirsky1 et al., 2011)
745 e 618	ρ(H_2O)(Wladimirsky1 et al., 2011)
495 e 456	δ ring(Wladimirsky1 et al., 2011)

meaning: ν = stretching, νas = antisymmetric stretching, νs = symmetric stretching, δ = bending, ρ = rocking. Source: Authors (2021).

According to Figure 3, For ZnOP, the characteristic band of the Zn-O bonding between 600 and 400 cm^{-1} is observed. However, for ZnO submitted to milling and leaching, it was observed the appearance of several bands, which were identified and related to the probable chemical groups responsible for such interactions, according to the FTIR spectra available in the literature for hydrated zinc oxalate (Table 2) (Cooper, 2015; Georgeta, Marcela, Anda, Gratiela, & Alexandrina, 2015; Wladimirsky, Palacios, María C. D'Antonio, & Ana C. González-Baró and Enrique J. Baran, 2011). In table 2 one can see the characteristic wavenumber of each spectral trace present in Figure 3 and its respective assignment. According to the mentioned literature of each attributed assignment, these bands can be of stretching, antisymmetric stretching, symmetric stretching, bending or rocking vibrations for the functional groups of the zinc oxalate hydrate. From the FTIR spectra, although the Z4L sample presented different x-ray diffraction peak, according to the infrared technique it presents the same chemical groups as the others, thus confirming the presence of interactions of the oxalate group with the zinc oxide used. To reverse the formation of zinc oxalate crystals formed during the acid leaching stage, it was performed for the Z3L sample (chosen as an intermediate between the milling times) the DSC/TG, presented in Figure 4 (a).

Figure 4 - (a) DSC/TG performed for the Z3L sample and (b) FTIR transmittance spectrum for ZnO P sample compared to the heat-treated ones.

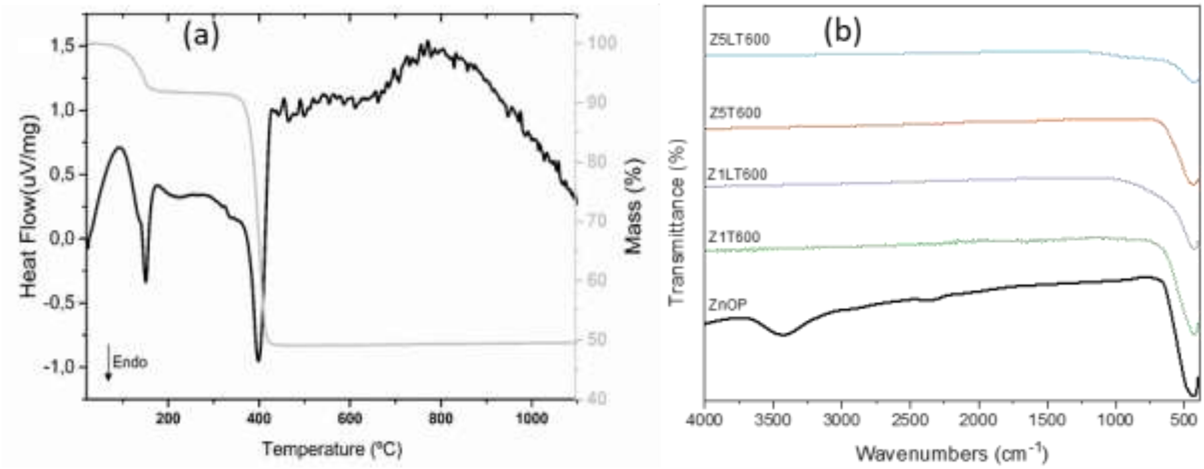

Source: Authors (2021).

According to Figure (a), there are two significant events showed by the coupling of the mass loss and heat flow curves: the presence of an endothermic peak at approximately 150ºC accompanied by a mass loss, corresponding to the vaporization of the hydration water; the second event, at 400ºC, also characterized by an endothermic peak accompanied by a significant mass loss corresponding to the decomposition of oxalate. Zinc oxalate can be thermally converted to zinc oxide after approximately 400 º C. Aiming to reverse the effect of the acid leaching a heat treatment at 600ºC was proposed for both samples: those submitted only to milling (also seeking to mitigate the effects of crystallinity loss due to HEBM) and the leached ones.

Figure 4 (b) shows the FTIR spectrum for the heat-treated samples. The ZnOP sample is presented just for comparison and shows a water band around 3383 cm^{-1}, which is absent on the other samples. Regarding the Zn-O bonding band, between 600 and 400 cm^{-1}, it is now present on the heat-treat samples and was not on the leached ones (Figure 3). It confirmed the heat treatment at 600 ºC was able to reverse the oxalic acid formation. Comparing the bands' intensity in Figure 4 (b), one can see that for both leached and heat-treated samples (Z1LT600 and Z5LT600), the Zn-O band, although present, was weaker than the just heat-treated ones. The intensity of the oxide bond was decreased according to the experimental procedures performed and had its lowest intensity for the sample leached and processed for the longest milling time. This fact corroborates the XRD analysis that the milling and the leaching processes led to deformations on the ZnO structure. Particle size distribution (Figure 5) by laser diffraction was performed for the samples milled for 2 and 5 h, before and after heat treatment at 600 ºC.

Figure 5 - Particle size distribution of the pattern powder, milled and heat-treated samples.

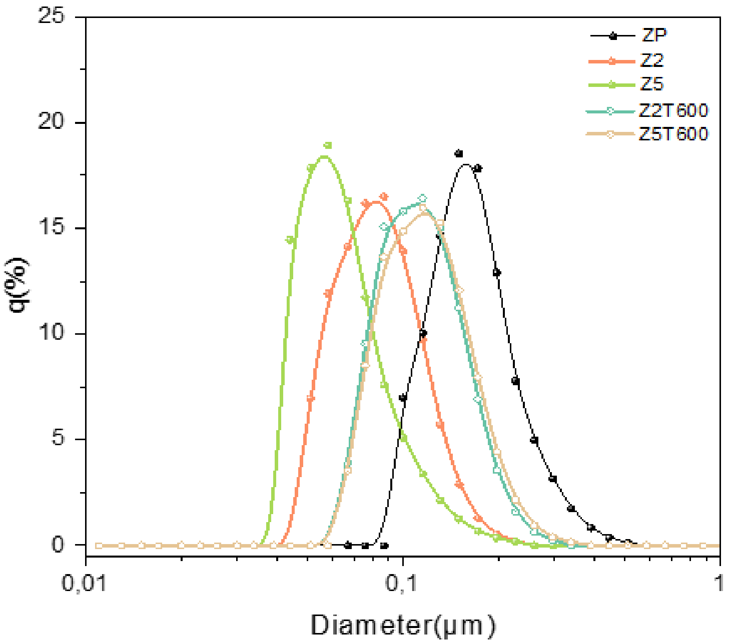

Source: Authors (2021).

The results showed in Figure 5 demonstrated the milling process was indeed able to reduce the particle size. When increasing the milling time from 2 to 5 h, the particle size was reduced completely to a nanometric scale (green curve), with an average size of approximately 50 nm. However, the heat treatment for both milling times provided the formation of aggregates and partially reversed the milling action, since the curves for the Z2T600 and Z5T600 showed particle size distribution in a higher scale. However, even with the heat treatment, the particle size did not reach the initial value of the ZnO precursor powder. To confirm the results of the presence of Fe, the X-ray fluorescence analysis is described in Table 3 for the samples processed for 2 and 5 h (Z2 and Z5).

Table 3 - Determinations of the compounds present in the samples by X-ray fluorescence.

Determinations (%)	**Samples**			
	Z2	Z2L	Z5	Z5L
Al_2O_3	0.16	0.39	0.6	0.32
SiO_2	0.15	0.23	0.14	0.28
Fe_2O_3	1.38	1.85	2.27	2.57
ZnO	98.30	97.53	97.00	96.80

Source: Authors (2021).

Comparing the leached samples obtained for both processing times according to the results presented in Table 3, an increase in the percentage values of the other compounds (Al_2O_3 and SiO_2) is observed. This fact can be explained, however, when observing the percentage values of ZnO. After acidic leaching, there was a decrease in the percentage of this oxide in the samples. This phenomenon suggests two events: the elimination of a small portion of ZnO solubilized in the acid during the leaching process and also the loss of some ZnO nanoparticles that have not been able to decant after the leaching. Therefore, the presence of Fe in the samples is confirmed even after the leaching process. It can also be noticed the increased in the Fe content according to the milling time, since Z2 presented 1.38% and Z5 presented 2.27%, indicating that an increase in 3 h of processing led to an increase of almost 65% of iron incorporation.

The SEM images of the precursor powder and the milled and leached powder are demonstrated in Figure 6 and 7, respectively.

Figure 6 - SEM image from the ZnO precursor powder.

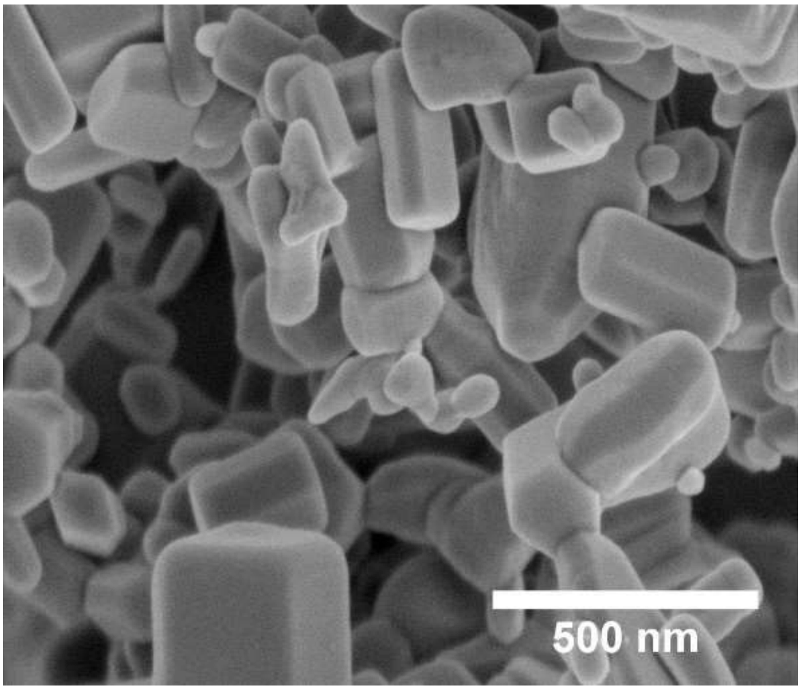

Source: Authors (2021).

The ZnO used as raw material consisted of particles predominantly on a submicron scale (between 100 and 600 nm, as shown in Figure 6). It can also be seen that the morphology of the particles is randomly shaped, more predominantly hexagonal prism and thin rods.

Figure 7 - SEM images for the ZnO powder milled for 2 and 5 h, and respective leached samples.

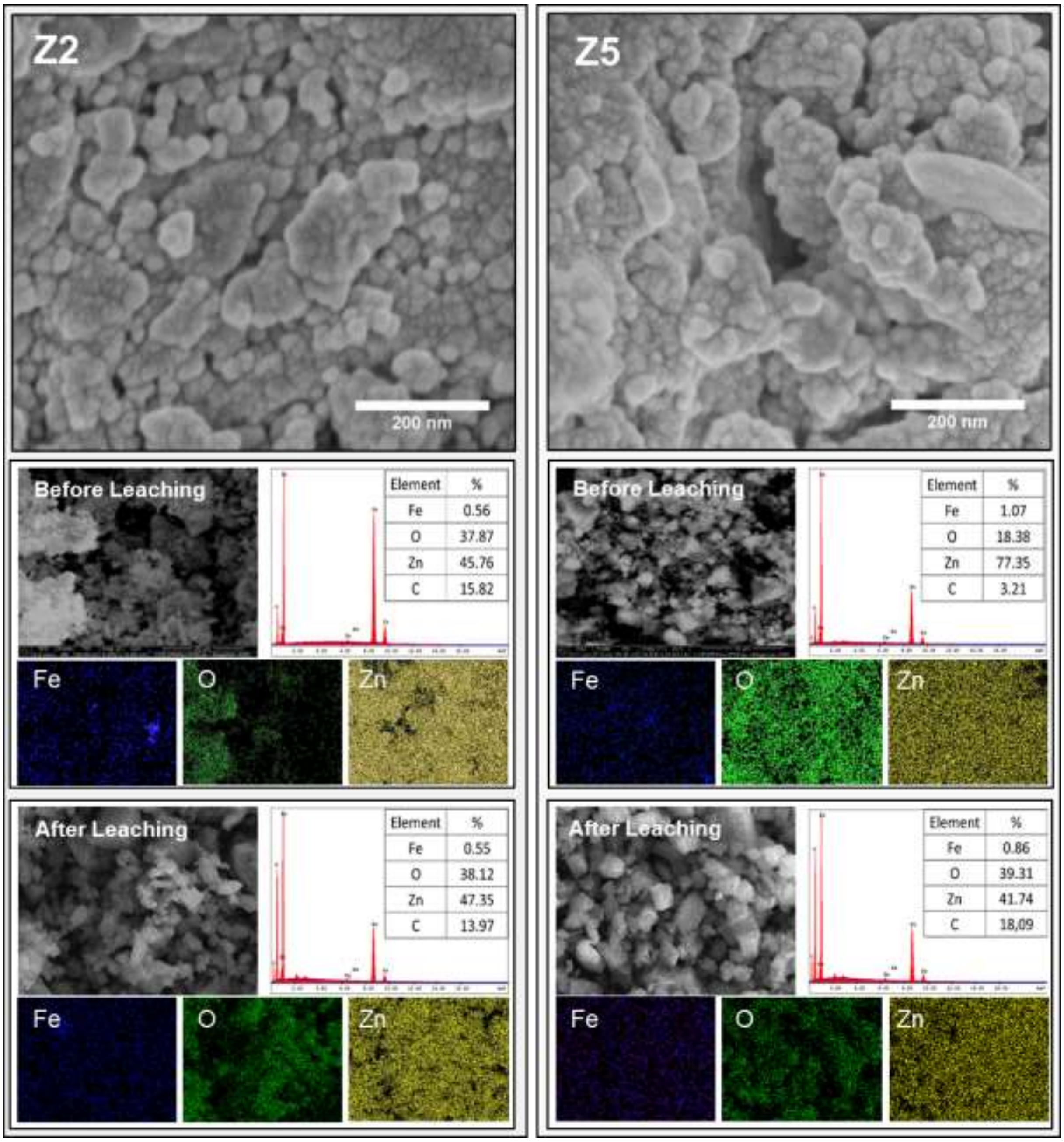

Element	%
Fe	0.56
O	37.87
Zn	45.76
C	15.82

Element	%
Fe	0.55
O	38.12
Zn	47.35
C	13.97

Element	%
Fe	1.07
O	18.38
Zn	77.35
C	3.21

Element	%
Fe	0.86
O	39.31
Zn	41.74
C	18,09

Source: Authors (2021).

For the SEM images of samples milled for 2 and 5 h, Figure 7 (a) and (b) respectively, presence of particles at the nanoscale and a wide distribution of agglomerates is observed, despite the deagglomeration methods adopted. To verify the dispersion of the constituent elements, analysis by energy dispersive spectroscopy (EDS) was performed together with element mapping for the 2 and 5 h milled samples (Z2 and Z5), before and after the leaching. The presence of the Fe element is perceived in all cases in a homogeneously dispersed manner throughout the analyzed region, confirming that it was not present in the form of isolated particles, according to the backscattered-electron analysis. The increase in milling time led to an increase in the percentage of Fe in the analyzed area. These results corroborate with those from Rietveld refinement and XRF. Long period of milling times favors the inclusion of Fe in the structure, leading to the lattice expansion. Also, Salah et al (2011) (Salah et al., 2011) reported changes on the morphology of the powder which was firstly random shapes to spherical shapes. This behavior was also reported in our work, where one can see by the SEM images the presence of spherical shapes rather than the hexagonal shapes presented by the precursor powder, which might also be useful for various applications. In order to verify the changes on the optical properties, the DRS spectra are shown in Figure 8.

Figure 8 - DRS spectra and Tauc's plots and the calculated band gap for the samples milled for 2 and 5 h.

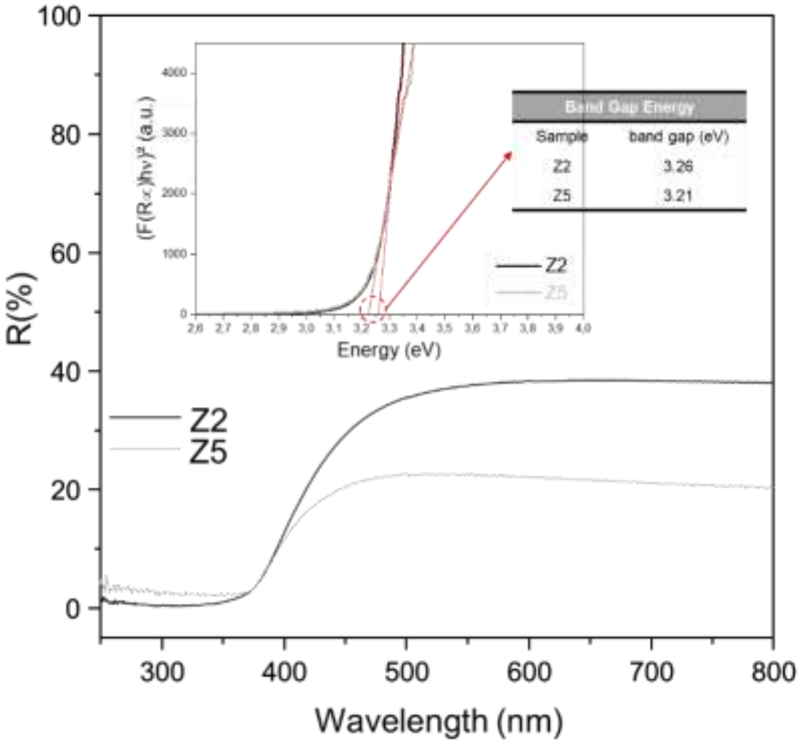

Source: Authors (2021).

The DRS spectra for the samples milled for 2 and 5 h (Figure 8), the added Tauc's plots and calculated band gap shows the influence of the milling process on the optical properties of ZnO. The ZnO presents an energy band gap of 3.37 eV and a wide absorption band at 370 nm. According to the Figure 8, There was a decrease on the reflectance intensity with an increase of the milling time. However, an increase of milling timing from 2 to 5 h decreased the band gap energy from 3.26 to 3.21 eV (from the inset graph), which leads to a lower energy requirement to be activated. No additional band appeared, demonstrating that no new phases came out with milling, as also demonstrated by the XRD results. Reddy et al (2019) (Reddy et al., 2019) studied the effect of Fe doped ZnO nanoparticles ball milled in a planetary mill on its optical property. The lowest optical band gap was achieved after 40h of milling, and the authors attributed the superior photocatalytic activity if the Fe doped ZnO to an increase in the electron-hole pair separation due to the inter charge diffusion between the bands. The presence of metal doping can substantially reduce the recombination rate of the photogenerated charge carriers in semiconductors (Akhundi & Habibi-Yangjeh, 2016; Shekofteh-Gohari & Habibi-Yangjeh, 2017). The high processing time could be reduced by replacing the planetary mill by the shaker mill (as used in this work), since the energy and frequency of impact is much higher in the latter (Suryanarayana, 2001).

As shown in previous works, interest in the applications of ZnO nanoparticles has grown in recent decades as it exhibits properties that can be applied to different fields, as biomedical, sensor and catalysis. The increased specific surface area and the reduced particle size leads to enhanced particle surface reactivity. Bottom-up approaches for obtaining nanoparticles (such as vapor synthesis, pyrolysis, sol–gel synthesis, and precipitation methods) are well stablished in the literature, enabling control of the particle size and morphology. However, for optimized conditions, these processes can present high complexity and costs. In this sense, top-down approaches (as mechanical milling) consist of a simple operation, coupled with low cost and possibility of high amounts of material been processed at the same time (S. Sharma, Pande, & Swaminathan, 2017). In relation to high energy ball milling, this is the first time in the literature that a shaker mill was applied to ZnO particle size reduction and physical characterization. High energy ball milling with a shaker mill proved to be suitable in achieving nanoparticles with great optical, physical and microstructure properties with a short time of processing. This could broaden the applicability of ZnO nanoparticles processed by HEBM, such as photocatalytic, antibacterial and antimicrobial applications. Also, crystallographic orientation plays an important rule regarding antibacterial activity and the paper also showed that an increase in the c value was able to be achieve in a reduced time compared to previous work with other milling type.

4. Conclusion

High energy milling using a shaker mill resulted in particle size reduction for both processing times with an increase in milling time. The oxalic acid leaching process presented strong interaction with the ZnO, leading to the formation of zinc oxalate which was reversed by heat treatment. The heat-treated powder, however, presented lower interaction between the Zn-O bond. Rietveld refinement showed the hexagonal structure progressively expanded according to milling time. Also, the c value increased, which might be useful for antibacterial and antimicrobial applications. The band-gap decreased to 3.21 V with 5h of milling, which might be useful for excitation events. High-energy milling using a shaker mill proved to be an efficient technique in reducing particle size in a significantly shorter processing time than other conventional mills.

HEBM showed how the process can promote structural changes and enhance the properties of the final processed powder. This process could help researches to overcome some challenges and future prospects to the field of nanostructured materials. Further investigations aiming at visible light applications to ZnO, by adding metal dopants (such as Sn, Mn, and Co) or semiconductors (such as TiO_2, SnO_2, and Co_3O_4) to the high energy milling process to form doped ZnO or ZnO heterostructures, respectively, can be an important route to broad and reduce the costs of ZnO application.

Acknowledgments

This study was financed by the Fundação de Amparo à Pesquisa do Estado de Minas Gerais (FAPEMIG) and Coordenação de Aperfeiçoamento de Pessoal de Nível Superior – Brasil, (CAPES -Finance Code 001). The authors also thank Jeferson Almeida Dias for his valuable contribution throughout the work, in particular regarding structural characterization

References

Aimable, A., Goure Doubi, H., Stuer, M., Zhao, Z., & Bowen, P. (2017). Synthesis and Sintering of ZnO Nanopowders. *Technologies*, 5(2), 28. https://doi.org/10.3390/technologies5020028

Akhundi, A., & Habibi-Yangjeh, A. (2016). Facile preparation of novel quaternary g-C3N4/Fe3O4/AgI/Bi2S3 nanocomposites: magnetically separable visible-light-driven photocatalysts with significantly enhanced activity. *RSC Advances,* 6(108), 106572–106583. https://doi.org/10.1039/c6ra12414c

Bégin-Colin, S., Gadalla, A., Le Caër, G., Humbert, O., Thomas, F., Barres, O., & Gilliot, P. (2009). On the origin of the decay of the photocatalytic activity of TiO 2 Powders ground at high energy. *Journal of Physical Chemistry C*, 113(38), 16589–16602. https://doi.org/10.1021/jp900108a

Chandekar, K. V., Shkir, M., Al-Shehri, B. M., AlFaify, S., Halor, R. G., Khan, A., & Hamdy, M. S. (2020). Visible light sensitive Cu doped ZnO: Facile synthesis, characterization and high photocatalytic response. *Materials Characterization,* 165(May), 110387. https://doi.org/10.1016/j.matchar.2020.110387

Chen, B., Xia, Z., & Lu, K. (2013). Understanding sintering characteristics of ZnO nanoparticles by FIB-SEM three-dimensional analysis. *Journal of the European Ceramic Society, 33*(13–14), 2499–2507. https://doi.org/10.1016/j.jeurceramsoc.2013.04.026

Chen, D., Wang, Z., Ren, T., Ding, H., Yao, W., Zong, R., & Zhu, Y. (2014). Influence of defects on the photocatalytic activity of ZnO. *Journal of Physical Chemistry C,* 118(28), 15300–15307. https://doi.org/10.1021/jp5033349

Choi, Y. I., Jung, H. J., Shin, W. G., & Sohn, Y. (2015). Band gap-engineered ZnO and Ag/ZnO by ball-milling method and their photocatalytic and Fenton-like photocatalytic activities. *Applied Surface Science,* 356(November), 615–625. https://doi.org/10.1016/j.apsusc.2015.08.118

Cooper, N. D. (2015). Complete Kinetic and Mechanistic Decomposition of Zinc Oxalate with Characterization of Intermediates and Final Oxide. Proceedings of the National Conference of Undergraduate Research.

Dias, J. A., Arantes, V. L., Ramos, A. S., Giraldi, T. R., Minucci, M. Z., & Maestrelli, S. C. (2016). Characterization and photocatalytic evaluation of ZnO–Co3O4 particles obtained by high energy milling. Part II: Photocatalytic properties. *Ceramics International,* 42(2), 3485–3490. https://doi.org/10.1016/j.ceramint.2015.10.151

Dias, J. A., Oliveira, J. A., Renda, C. G., & Morelli, M. R. (2018). Production of Nanometric Bi4Ti3O 12 Powders: from Synthesis to Optical and Dielectric Properties. *Materials Research,* 21(5). https://doi.org/10.1590/1980-5373-mr-2018-0118

Dib, K., Trari, M., & Bessekhouad, Y. (2020). (S,C) co-doped ZnO properties and enhanced photocatalytic activity. *Applied Surface Science*, 505(July 2019), 144541. https://doi.org/10.1016/j.apsusc.2019.144541

Dutková, E., Sayagués, M. J., Briančin, J., Zorkovská, A., Bujňáková, Z., Kováč, J., & Ficeriová, J. (2016). Synthesis and characterization of CuInS2 nanocrystalline semiconductor prepared by high-energy milling. *Journal of Materials Science*, 51(4), 1978–1984. https://doi.org/10.1007/s10853-015-9507-x

Dzik, P., Svoboda, T., Kaštyl, J., & Veselý, M. (2019). Modification of photocatalyst morphology by ball milling and its impact on the physicochemical properties of wet coated layers. *Catalysis Today,* 328(July 2018), 65–70. https://doi.org/10.1016/j.cattod.2019.01.051

Fan, J. C., Sreekanth, K. M., Xie, Z., Chang, S. L., & Rao, K. V. (2013). p-Type ZnO materials: Theory, growth, properties and devices. *Progress in Materials Science*, 58(6), 874–985. https://doi.org/10.1016/j.pmatsci.2013.03.002

Gancheva, M. N., Iordanova, R. S., Dimitriev, Y. B., Avdeev, G. V., & Iliev, T. C. (2013). Effects of mechanical activation on structure and photocatalytic properties of ZnO powders. *Central European Journal of Chemistry*, 11(11), 1780–1785. https://doi.org/10.2478/s11532-013-0314-4

Georgeta, G., Marcela, S., Anda, P., Gratiela, I., & Alexandrina, F. (2015). Comparative study on the recovery of zinc, cadmium and lead cations from waste waters using precipitation method. XXIV, 155–162.

Gonçalves, N. P. F., Paganini, M. C., Armillotta, P., Cerrato, E., & Calza, P. (2019). The effect of cobalt doping on the efficiency of semiconductor oxides in the photocatalytic water remediation. *Journal of Environmental Chemical Engineering*, 7(6). https://doi.org/10.1016/j.jece.2019.103475

Güler, S. H., Güler, Ö., Evin, E., & Islak, S. (2016). Electrical and optical properties of ZnO-milled Fe2O3 nanocomposites produced by powder metallurgy route. *Optik*, 127(6), 3187–3191. https://doi.org/10.1016/j.ijleo.2015.12.103

Hernández, R. A. H., García, F. L., Cruz, L. E. H., & Luévanos, A. M. (2013). Iron removal from a kaolinitic clay by leaching to obtain high whiteness index. *IOP Conference Series: Materials Science and Engineering*, *45*(1). https://doi.org/10.1088/1757-899X/45/1/012002

Jiang, J., Mu, Z., Xing, H., Wu, Q., Yue, X., & Lin, Y. (2019). Insights into the synergetic effect for enhanced UV/visible-light activated photodegradation activity via Cu-ZnO photocatalyst. *Applied Surface Science*, 478(January), 1037–1045. https://doi.org/10.1016/j.apsusc.2019.02.019

Khalid, N. R., Hammad, A., Tahir, M. B., Rafique, M., Iqbal, T., Nabi, G., & Hussain, M. K. (2019). Enhanced photocatalytic activity of Al and Fe co-doped ZnO nanorods for methylene blue degradation. *Ceramics International,* 45(17), 21430–21435. https://doi.org/10.1016/j.ceramint.2019.07.132

Kotha, V., Kumar, K., Dayman, P., & Panchakarla, L. S. (2021). Doping with Chemically Hard Elements to Improve Photocatalytic Properties of ZnO Nanostructures. *Journal of Cluster Science*, 3, 41–45. https://doi.org/10.1007/s10876-021-02115-3

Kumar, Pawan, & Kumar, R. (2021). Synthesis process of functionalized ZnO nanostructure for additive manufacturing: a state-of-the-art review. In Additive Manufacturing with Functionalized Nanomaterials. https://doi.org/10.1016/b978-0-12-823152-4.00002-8

Kumar, Promod, Kumar, A., Rizvi, M. A., Moosvi, S. K., Krishnan, V., Duvenhage, M. M., & Swart, H. C. (2020). Surface, optical and photocatalytic properties of Rb doped ZnO nanoparticles. *Applied Surface Science,* 514(February), 145930. https://doi.org/10.1016/j.apsusc.2020.145930

Lee, K. M., Lai, C. W., Ngai, K. S., & Juan, J. C. (2016). Recent developments of zinc oxide based photocatalyst in water treatment technology: A review. *Water Research*, 88, 428–448. https://doi.org/10.1016/j.watres.2015.09.045

Lott, K., Nirk, T., Gorokhova, E., Türn, L., Viljus, M., Öpik, A., & Vishnjakov, A. (2015). High temperature electrical conductivity in undoped ceramic ZnO. *Crystal Research and Technology,* 50(1), 10–14. https://doi.org/10.1002/crat.201400138

Mayo, M. J., Hague, D. C., & Chen, D.-J. (1993). Processing nanocrystalline ceramics for applications in superplasticity. *Materials Science and Engineering:* A, 166(1–2), 145–159. https://doi.org/10.1016/0921-5093(93)90318-9

Mekprasart, W., Chutipaijit, S., Ravuri, B. R., & Pecharapa, W. (2020). Antibacterial activity of yellow zinc oxide prepared by high-energy ball milling technique. AIP Conference Proceedings, 2279(October). https://doi.org/10.1063/5.0027955

Morkoç, H., & Özgür, Ü. (2009). Zinc Oxide: Fundamentals, Materials and Device Technology. https://doi.org/10.1002/9783527623945

Mote, V., Purushotham, Y., & Dole, B. (2012). Williamson-Hall analysis in estimation of lattice strain in nanometer-sized ZnO particles. *Journal of Theoretical and Applied Physics*, 6(1), 6. https://doi.org/10.1186/2251-7235-6-6

Noman, M. T., Amor, N., & Petru, M. (2021). Synthesis and applications of ZnO nanostructures (ZONSs): a review. Critical Reviews in Solid State and *Materials Sciences, 0*(0), 1–43. https://doi.org/10.1080/10408436.2021.1886041

Otis, G., Ejgenberg, M., & Mastai, Y. (2021). Solvent-free mechanochemical synthesis of zno nanoparticles by high-energy ball milling of ε-zn(Oh)2 crystals. *Nanomaterials*, 11(1), 1–12. https://doi.org/10.3390/nano11010238

Pallone, E. M. de J. A., Trombini, V., Silva, K. L., Bernardi, L. O., Yokoyama, M., & Tomasi, R. (2010). Production and Characterization of Alumina-Diamond Composites and Nanocomposites. *Advances in Science and Technology*, *65*, 16–20. https://doi.org/10.4028/www.scientific.net/AST.65.16

Phuah, X. L., Rheinheimer, W., Akriti, Dou, L., & Wang, H. (2021). Formation of liquid phase and nanostructures in flash sintered ZnO. *Scripta Materialia*, 195, 113719. https://doi.org/10.1016/j.scriptamat.2020.113719

Poornaprakash, B., Chalapathi, U., Subramanyam, K., Vattikuti, S. V. P., & Park, S. H. (2020). Wurtzite phase Co-doped ZnO nanorods: Morphological, structural, optical, magnetic, and enhanced photocatalytic characteristics. *Ceramics International*, 46(3), 2931–2939. https://doi.org/10.1016/j.ceramint.2019.09.289

Prabhu, Y. T., Rao, K. V., Kumar, V. S. S., & Kumari, B. S. (2014). X-Ray Analysis by Williamson-Hall and Size-Strain Plot Methods of ZnO Nanoparticles with Fuel Variation. *World Journal of Nano Science and Engineering*, 04(01), 21–28. https://doi.org/10.4236/wjnse.2014.41004

Qin, X. J., Shao, G. J., Liu, R. P., & Wang, W. K. (2005). Sintering characteristics of nanocrystalline ZnO. *Journal of Materials Science*, 40(18), 4943–4946. https://doi.org/10.1007/s10853-005-3874-7

Reddy, I. N., Reddy, C. V., Sreedhar, M., Shim, J., Cho, M., & Kim, D. (2019). Effect of ball milling on optical properties and visible photocatalytic activity of Fe doped ZnO nanoparticles. Materials Science and Engineering B: Solid-State Materials for Advanced Technology, 240(October 2017), 33–40. https://doi.org/10.1016/j.mseb.2019.01.002

Salah, N., Habib, S. S., Khan, Z. H., Memic, A., Azam, A., Alarfaj, E., & Al-Hamedi, S. (2011). High-energy ball milling technique for ZnO nanoparticles as antibacterial material. *International Journal of Nanomedicine*, 6, 863–869. https://doi.org/10.2147/ijn.s18267

Saleh, R., Prakoso, S. P., & Fishli, A. (2012). The influence of Fe doping on the structural, magnetic and optical properties of nanocrystalline ZnO particles. *Journal of Magnetism and Magnetic Materials*, 324(5), 665–670. https://doi.org/10.1016/j.jmmm.2011.07.059

Samavati, A., Awang, A., Samavati, Z., Fauzi Ismail, A., Othman, M. H. D., Velashjerdi, M., & Rostami, A. (2021). Influence of ZnO nanostructure configuration on tailoring the optical bandgap: Theory and experiment. Materials Science and Engineering B: Solid-State Materials for Advanced Technology, 263(August 2020), 114811. https://doi.org/10.1016/j.mseb.2020.114811

Schreyer, M., Guo, L., Thirunahari, S., Gao, F., & Garland, M. (2014). Simultaneous determination of several crystal structures from powder mixtures: the combination of powder X-ray diffraction, band-target entropy minimization and Rietveld methods. *Journal of Applied Crystallography*, 47(2), 659–667. https://doi.org/10.1107/S1600576714003379

Šepelák, V., Bégin-Colin, S., & Le Caër, G. (2012). Transformations in oxides induced by high-energy ball-milling. *Dalton Transactions*, 41(39), 11927–11948. https://doi.org/10.1039/c2dt30349c

Shannon, R. D. (2011). Radii for All Species. http://abulafia.mt.ic.ac.uk/shannon/radius.php#R

Sharma, N., Jandaik, S., & Kumar, S. (2016). Synergistic activity of doped zinc oxide nanoparticles with antibiotics: Ciprofloxacin, ampicillin, fluconazole and amphotericin B against pathogenic microorganisms. Anais Da Academia Brasileira de Ciencias, 88(3), 1689–1698. https://doi.org/10.1590/0001-3765201620150713

Sharma, S., Pande, S. S., & Swaminathan, P. (2017). Top-down synthesis of zinc oxide based inks for inkjet printing. *RSC Advances*, 7(63), 39411–39419. https://doi.org/10.1039/c7ra07150g

Shekofteh-Gohari, M., & Habibi-Yangjeh, A. (2017). Fe3O4/ZnO/CoWO4 nanocomposites: Novel magnetically separable visible-light-driven photocatalysts with enhanced activity in degradation of different dye pollutants. *Ceramics International*, 43(3), 3063–3071. https://doi.org/10.1016/j.ceramint.2016.11.115

Silva, K. L., Bernardi, L. O., Yokoyama, M., Trombini, V., Cairo, C. A., & Pallone, E. M. J. A. (2008). Obtained of diamond nanometric powders using high energy milling for the production of alumina-diamond nanocomposites. *Materials Science Forum*, *591–593*, 766–770. https://doi.org/10.4028/www.scientific.net/msf.591-593.766

Suryanarayana, C. (2001). Mechanical alloying and milling. *Progress in Materials Science*, 46(1–2), 1–184. https://doi.org/10.1016/S0079-6425(99)00010-9

Toporovska, L., Turko, B., Savchak, M., Seyedi, M., Luzinov, I., Kostruba, A., & Vaskiv, A. (2020). Zinc oxide: reduced graphene oxide nanocomposite film for heterogeneous photocatalysis. *Optical and Quantum Electronics*, 52(1), 1–12. https://doi.org/10.1007/s11082-019-2132-1

Wang, X., Zhu, Y., Huang, R., Mei, H., & Jia, Z. (2019). Flash sintering of ZnO ceramics at 50 °C under an AC field. *Ceramics International*, 45(18), 24909–24913. https://doi.org/10.1016/j.ceramint.2019.08.142

Williamson, G., & Hall, W. (1953). X-ray line broadening from filed aluminium and wolfram. *Acta Metallurgica*, 1(1), 22–31. https://doi.org/10.1016/0001-6160(53)90006-6

Wladimirsky, A., Palacios, D., María C. D'Antonio, González-Baró, A. C., & Baran, E. J. (2011). Vibrational spectra of the α-MIIC2O4·2H2O oxalato complexes, with MII = Co, Ni, Zn. *Journal of the Argentine Chemical Society*, 98, 71–77. https://doi.org/10.1107/S010827010400l945/sk1664sup1.cif

Yamamoto, O., Komatsu, M., Sawai, J., & Nakagawa, Z. E. (2004). Effect of lattice constant of zinc oxide on antibacterial characteristics. Journal of Materials Science: *Materials in Medicine*, 15(8), 847–851. https://doi.org/10.1023/B:JMSM.0000036271.35440.36

Yin, L., Zhang, D., Wang, J., Huang, J., Kong, X., Fang, J., & Zhang, F. (2017). Improving sunlight-driven photocatalytic activity of ZnO nanostructures upon decoration with Fe(III) cocatalyst. *Materials Characterization*, 127, 179–184. https://doi.org/10.1016/j.matchar.2017.03.004

Yokoyama, M. (2008). Dissertation Thesis - *Obtenção e Caracterização de compósitos e nanocompositos de alumina-diamante*. Universidade São Francisco.

Zhang, X., Qin, J., Xue, Y., Yu, P., Zhang, B., Wang, L., & Liu, R. (2014). Effect of aspect ratio and surface defects on the photocatalytic activity of ZnO nanorods. *Scientific Reports*, 4, 4–11. https://doi.org/10.1038/srep04596